On the role of support in metallic heterogeneous catalysis: A study of unsupported Nickel-Cobalt alloy nanoparticles in ethanol steam reforming.

Gabriella Garbarino[a,b], Tullio Cavattoni[c], Paola Riani [b,d*], Rosaria Brescia[e], Fabio Canepa[c], and Guido Busca[a,b]

[a] Università degli Studi di Genova, Dipartimento di Ingegneria Civile, Chimica e Ambientale (DICCA), Laboratorio di chimica delle superfici e catalisi, Via all'Opera Pia 15, 16145, Italy

[b] INSTM, UdR Genova, Via Dodecaneso, 31 16146 Genova, Italy

[c] Università degli Studi di Genova, Dipartimento di Chimica e Chimica Industriale (DCCI), Via Dodecaneso, 31 16146 Genova, Italy

[d] Università degli Studi di Genova, Dipartimento di Farmacia (DIFAR), Viale Cembrano 4 16148 Genova, Italy

[e] Electron Microscopy Facility, Istituto Italiano di Tecnologia (IIT), Via Morego 30, 16163 Genova, Italy

Corresponding author: email paola.riani@unige.it tel +39 010 353-6174 fax: +39 010 353-8733 - Università degli Studi di Genova, Dipartimento di Farmacia (DIFAR), Viale Cembrano 4 16148 Genova, Italy

Abstract

(Co,Ni) bimetallic nanoparticles have been prepared by reducing Ni and Co chloride solutions with sodium borohydride. The obtained materials have been characterized as cast and/or after annealing by means of XRD, magnetic measurements, IR spectroscopy, FESEM and TEM microscopies. The resulting nanomaterials, originally amorphous, crystallize into the cubic structure cF4-Cu as homogeneous (Co,Ni) solid solution alloy and with the additional presence of Boron containing phases due to the residual preparation impurities. The bimetallic nanoparticles are active in ethanol conversion in the presence of steam. For low Boron catalysts, the addition of Nickel to Cobalt nanoparticles improves the catalytic activity in ethanol steam reforming allowing yields as high as 87 % at 773 K, at high space velocities (GHSV 324000 h^{-1}). The performances of the catalytic unsupported nanoparticles with a Ni/Co atomic ratio equal to 0.26 appear to be better than those of conventional supported catalysts. The state of Boron impurities affect catalytic activity of bimetallic (Co,Ni) NPs. Carbonaceous materials, such as carbon nanotubes and graphitic carbon, form on the catalyst surface upon reaction.

Keywords: Ethanol Steam Reforming; bimetallic nanoparticles; Cobalt; Nickel; heterogeneous catalysts

1. Introduction.

Metals represent a main family of heterogeneous catalysts, largely applied for hydrogenations, oxidations and steam reforming processes [1]. Most of industrial metallic catalysts are supported [2]: in fact, carriers such as high-surface area metal oxides (alumina, silica, zirconia, titania, alkali earth aluminates, zeolites, etc.) or carbon materials are supposed to produce more reactive nanoparticles, but may also allow stabilizing metallic particles against sintering [3]. Unsupported metals are also applied in some cases, such as iron for ammonia synthesis and for the Fischer Trøpsch reaction, Nickel Raney for liquid phase hydrogenations, etc. These materials are in the form of relatively large porous particles and contain impurities that actually activate and stabilize them.

BioE-ethanol Steam Reforming (ESR) is a potentially useful process for producing renewable hydrogen and syngas ~~starting from bioethanol~~ [4,5]. While supported noble metals (Pt, Rh, ..) are most active for steam reforming (SR) processes, supported Ni catalysts are most commonly considered, due to their good activity, robustness and low cost. However, in the case of ESR, supported cobalt catalysts may be even more active than supported nickel catalysts in particular at low temperature [6,7]. Concerning conventional supported catalysts, we previously found that alloying Nickel with Cobalt [8,9,10,11,12] may produce even better catalysts than monometallic ones for ESR.

The nature of the support has also been reported to have a considerable effect on the activity of the metal [6,13,14]. On the other hand we have also found that unsupported nickel [15] and cobalt nanoparticles [16,17,18] have very high activity. In this case cobalt catalysts also show high hydrogen selectivity associated to a very reduced coproduction of methane.

In this paper, we report on our efforts to produce unsupported (Co,Ni) nanoparticles, and on their activity as catalysts for Ethanol Steam Reforming. The aims of this work are: i) to check the role of the support in the ESR reaction; ii) to check the effect of the preparation procedure on the resulting (Co,Ni) nanomaterials; iii) to evaluate the effect of the bimetallic formulation and on the role of boron impurities in a complex system; and iii) to elucidate the chemistry of the ESR process for (Co,Ni) NPs.

2. Experimental.

2.1. NPs preparation of bimetallic nanoparticles.

The (Co,Ni) nanoparticles were prepared via reduction method in aqueous solution, starting from $NiCl_2 \cdot 6H_2O$, $CoCl_2 \cdot 6H_2O$ and using $NaBH_4$ as reducing agent. The reaction was carried

out using a 1:1 (samples A, B, C, D, E) or 2:1 (sample F) or a 4:1 (sample G) concentration ratio between Co(II) and Ni(II) chloride salts, in order to reach a final concentration of 10^{-2} M for metals in solution, with a Me^{2+}:BH_4^- ratio equal to 1:2.

The aqueous salt solution was kept under vigorous mechanical stirring in Argon atmosphere; once obtained a good homogeneity, sodium borohydride was added. Its addition caused a rapid change in the solution color that turned into black, confirming the appearance of the nanoparticles. The reaction mixture was maintained under vigorous mechanical stirring for 15 minutes, then the (Co,Ni) NPs were collected using different methods (centrifugation sample D, filtration samples A, B, F, G, filtration followed by sonication samples C, E), washed several times and, finally, dried and stored in dynamic vacuum.

As already observed for Co NPs [16~~14~~,17~~15~~,18~~16~~] the washing procedure strongly affects the purity of the sample. This is related to the adopted reducing agent that could leave boron in the final product, thus producing metal borides together or instead of the corresponding metals. This inconvenient can be avoided by washing in open air, thus converting the boron impurities into borates, which can be then removed during the washes with water.

The notation of the samples and their main characteristics are summarized in Table 1.

2.2 Materials characterisation

X-ray diffraction patterns on dried nanoparticles, annealed at 773 K for 3 hours in argon atmosphere, and on the exhaust samples (after the catalytic tests) were carried out by using a vertical powder diffractometer X'Pert with Cu Kα radiation (λ = 0.15406 nm). The patterns were usually collected in the 25 – 100° 2θ range with a step of 0.02° and a counting time for each step of at least 12 s. Powder patterns were indexed by comparing experimental results to the data reported in the Pearson's Crystal Data database [19].

IR spectra were recorded with ThermoFisher Instrument using KBr pressed disks (1% wt/wt of sample, total weight 0.8080g). In the related figures they are reported in common scale but shifted for clarity of imaging.

A scanning electron microscope ZEISS SUPRA 40 VP, with a field emission gun, was used to study the morphology of all the prepared catalysts (FE-SEM measurements). This instrument is equipped with a high sensitivity "InLens" secondary electrons detector and with an energy-dispersive X-ray spectroscopy (EDX) microanalysis OXFORD "INCA Energie

450x3". For SEM analysis, the samples were suspended in ethanol and exposed to ultrasonic vibrations to decrease the aggregation. A drop of the resultant mixture was finally laid on a Lacey Carbon copper grid.

Samples for TEM examinations were prepared just after breaking vacuum (sealed glass pipe); few mg of each sample were sonicated in ethanol, then deposited onto a double amorphous carbon film-coated (ultrathin film on holey film) Cu TEM grid.
Energy-filtered TEM (EFTEM) and high angle annular dark field-scanning TEM (HAADF-STEM) imaging and STEM-EDX analyses were carried out using an image-C_s-corrected JEOL JEM-2200FS TEM (Schottky emitter, operated at 200 kV), equipped with an in-column filter (Ω-type) and a Bruker silicon-drift detector (XFlash 5060) for EDX.

STEM-EDX maps were computed by integrating the B Kα, O Kα, Co Kα and Ni Kα X-ray peaks. EELS quantification was carried out on the background-subtracted and plural scattering-deconvolved spectra using the software EELSModel software [20].

DC magnetization was performed in a dc-Superconducting Quantum Interference Device (SQUID) magnetometer (MPMS—Magnetic Properties Measurement System, Quantum Design) with resolution better than 10^{-6} emu (RSO option). The room temperature (RT) magnetic hysteresis cycle was obtained in the 0–5 Tesla (T) $\mu_0 H$ magnetic field range.

2.3 Catalytic activity

The catalytic experiments were carried out in a flow fixed-bed tubular silica glass reactor. The reactor has been loaded with 7.4 mg of catalyst mixed with 476.7 mg of silica glass particles (60-70 mesh sieved) and when the Gas Hourly Space Velocity (GHSV) effect was investigated, 44.1 mg of catalyst were mixed with 440 mg of silica glass, in order to maintain the same reactor volume. The fed gas had the following composition 8.3% ethanol, 50.1% H_2O and 41.6% helium giving rise to GHSV values of 324000 h^{-1} and 51700 h^{-1} respectively, calculated on the catalyst volume. The reaction temperature was varied as follows: 523 K → 573 K → 673 K → 773 K → 673 K→ 573 K → 523 K, with the reaction held at each temperature for 1 h.
Product analysis was performed with a gas-chromatograph Agilent 4890 equipped with a Varian capillary column “Molsieve 5A/Porabond Q Tandem” and TCD and FID detectors in series. Between them a nickel catalyst tube was employed to reduce CO_x to CH_4. Products analysis was also performed on GC/MS (FOCUS and ISQ from Thermo-Fisher), in order to

have a precise identification of the compounds. The conversion of the reactants is defined as follows :

(1) $$X_{reactant} = \frac{nreact.in - nreact.out}{nreact.in}$$

while selectivity to C-product *i* is defined as:

(2) $$S_i = \frac{n_i}{\nu_i(nreact.in - nreact.out)}$$

where n_i is the number of moles in compound i, and ν_i is the ratio of stoichiometric reaction coefficients. The hydrogen yield is defined as:

(3) $$Y_{H2} = \frac{n_{H2\ out}}{6*(n_{ethanol\ in})}$$

3. Results and discussion

3.1. Separation, behavior and characterization of catalyst D, separated by centrifugation

The separation of the (Co,Ni) NPs from the reaction medium has been performed through centrifugation carried out applying the following process parameters 7500 rpm and a total time of 15 min, followed by washing in deionized water, then in ethanol and drying under vacuum. According to previous indications, this procedure guarantees a long contact time between nanoparticles and an oxidizing atmosphere, thus producing the conversion of boron in the borides to borates as much as possible. The sample has been characterized by means of XRD before annealing (not shown), providing evidence of a complete amorphicity of the sample, and after annealing in Ar at 773 K for 3 h. In this case (Figure 1), crystalline $B_2O_6M_3$ (M=Ni, Co) with an orthorhombic structure pertaining to space group number 58 (oP22, $Mg_3(BO_3)_2$ type) is present together with the features of cubic metallic (Ni,Co) solid solution (cF4-Cu type). FE-SEM micrograph identifies (Co,Ni) NPs of the order of 50 nm (not shown here) with a Co/O=Ni/O≈ 0.2 atomic ratio, obtained by EDX, demonstrating again the compresence of both metals and the quite high oxygen content, suitable with the results coming from other techniques. The high oxygen presence is confirmed by the presence of borates by IR spectroscopy (Figure 2) characterized by the features in the region 1500-1200 cm^{-1} and 900-700 cm^{-1} due to borates with different configurations (i.e. planar and tetrahedral) [21,22,23]. Planar BO_3^{3-} groups are characterised by asymmetric and symmetric B-O stretching in the 1500-1200 cm^{-1} and 1000-900 cm^{-1} regions respectively; instead, in-plane and an out-of-plane bending modes are found near 740 and 650 cm^{-1}. Tetrahedral

borate species have characteristic asymmetric and symmetric B-O stretchings in the region 1100-900 cm^{-1} [21~~25~~,22~~26~~]. Similar features have been also found for nanosized Cobalt catalysts for the $NaBH_4$ hydrolysis [23~~27~~], for the unsupported [16~~14~~,17~~15~~] and for supported CoNPs [18~~16~~].

3.2. Separation, behavior and characterization of catalysts C and E, separated by filtration and successive washing in deionized water for three times

The separation of the (Co,Ni) NPs from the reaction medium has been performed through filtration and successive washing in deionized water for three times. Then (Co,Ni) NPs were dispersed in 20 ml of absolute ethanol (>99.8%) and sonicated under Argon flow for 1 minute, in order to convert all eventual borides to borate species and thus enhancing the production of amorphous (Co,Ni) metallic NPs. Two samples have been prepared and characterized to evaluate data reproducibility. In this case, the XRD pattern of the annealed samples (Figure 1) shows only the characteristic peaks of metallic (Co,Ni) cubic alloy. A representative peak (2theta=76.3°) has been magnified in inset of Fig. 1 showing that the maximum is in-between the peaks of pure annealed Co and Ni metals. In Figure 3, FE-SEM micrographs show (Co,Ni) NPs with a maximum diameter of ≈20 nm; their composition has been obtained by SEM-EDX analysis and has been quantified by a Co/Ni=1 and a Co/O= Ni/O= 2.0 (average on 10 spots) atomic ratio, for both samples. HAADF-STEM images confirmed the morphology observed at FE-SEM (Fig. 4a). The STEM-EDX elemental maps show a slightly Ni-richer surface and a Co-rich core of the NP agglomerates. Moreover, elemental quantification carried out by STEM-EDX (three areas including a large number of NPs) indicates the presence of B (B/Co=0.42), and the atomic ratio between Co and Ni inside the nanoparticles (Ni/Co=0.99), thus confirming the achievement of the proper stoichiometric ratio. The results of IR analysis (see Fig. 2) confirm, for both samples, the goodness of our method showing the typical features of borates species with a lower intensity than that observed in the previous case(sample D).

3.3. Separation, behavior and characterization of catalyst B, separated by filtration and successive washing in deionized water for ten times.

The separation of the (Co,Ni) NPs from the reaction medium has been performed through filtration and successive washing in deionized water for ten times, in order to remove all the

anions and cations from the reducing agent and salt precursor, i.e. Na^+ and Cl^-. Then the sample has been dried under dynamic vacuum. The annealed sample (Fig. 1) shows the characteristic diffraction pattern of the orthorhombic BMe_3 (Me=(Co,Ni) oP16, Fe_3C) together with the features of cubic metallic (Ni,Co) solid solution (cF4-Cu type). The BMe_3 presence might be explained by taking into account the complex solid state reactions network (reaction 1 and 2) reported in the literature [24,25] occurring at 773 K and in inert atmosphere for Co based materials, supposing that also Ni gives rise to the same reactions pathways (1 and 2, where Me=Co, Ni).

$$2Me_2B + Me(BO_2)_2 \rightarrow 5Me + 2B_2O_x \quad (1)$$

$$Me_2B + Me \rightarrow Me_3B \quad (2)$$

FE-SEM micrograph (Fig. 3b) identifies (Co,Ni) NPs with a maximum diameter of 20 nm and with a Co/O=0.8 and Ni/O=0.5 atomic ratio, obtained by SEM-EDX analysis. HAADF-STEM images confirmed the morphology observed at FE-SEM (Fig. 4b) and also the spatial distribution of Co and Ni over the NPs observed in the sample C.

Elemental quantification carried out by STEM-EDX indicates the presence of a higher B content compared to sample C (B/Co=B/Ni≈1), also confirmed by the absorbance value of the borates peaks measured at IR, and the achievement of the proper stoichiometric ratio between Co and Ni inside the nanoparticles (Ni/Co=1).

In Figure 2, IR spectra of fresh sample B is reported and the typical feature for borates are still well detectable according to the fingerprint bands at 1400, 1100 and 950 cm^{-1}. The band at 1400 cm^{-1} has a comparable absorbance to the one of C.

3.4. Separation, behavior and characterization of catalysts A, F and G, separated by filtration and successive washing in deionized water for three times and dried under dynamic vacuum

The separation of the (Co,Ni) NPs from the reaction medium has been performed through filtration and successive washing in deionized water for three times and dried under dynamic vacuum, in order to prevent NPs oxidation. In this case, the preparation have been performed for three different concentration ratios between Co(II) and Ni(II) chloride salts: 1:1 for sample A, 2:1 for sample F and 4:1 for sample G, always preserving the final concentration of 10^{-2} M for metals in solution, with a ratio Me^{2+}:BH_4^- equal to 1:2. The different stoichiometric ratios have been chosen in order to study the effect of the different Ni/Co ratio on the catalytic activity.

In Figure 1 (samples F and G), the annealed samples show the same peaks BMe_3 (Me=(Co,Ni) oP16, Fe_3C) together with the features of cubic metallic (Co,Ni) solid solution (cF4-Cu type). In this case, the sample seems to be enriched in the cubic metal phase with respect to sample B that are similar to the pattern of A (not reported, since good data reproducibility as evidenced for E and C). In Figure 3d, FE-SEM micrograph of sample G (reported as meaningful example) identifies (Co,Ni) NPs with a maximum diameter of 20 nm and with a Co/O=Ni/O≈3 ratio, obtained by SEM-EDX analysis. This datum well compare with the IR analysis (Figure 2) that shows relatively broad features for borates species.
Elastically-filtered (zero-loss) TEM and HAADF-STEM images of these samples (Figure 5 a,b,c), respectively, confirm the morphology observed by FE-SEM.
Elemental quantification indicates, for all the three samples, the presence of a high B content (B/Co=B/Ni=1) and the Co/Ni atomic ratio within the nanoparticles (Ni/Co=1 for A, assessed by STEM-EDX, and Ni/Co=0.26 for G and Ni/Co=0.52 for F, the latter two assessed by EELS).

3.5 Magnetic measurements

In Figure 6, the room temperature magnetic hysteresis cycles of two representative samples, namely E and A, are reported. Both samples display the same anhysteretic behavior with no saturation magnetization reached at the highest explored field ($\mu_0 H$ = 5 Tesla). Very low values of the coercive field are reached for the two samples, namely 2 Oe (0.2 mT) and 9 Oe (0.9 mT) for samples E and A, respectively. Both systems are, thus, in the superparamagnetic regime, confirming the very small dimensions of the nanoparticles.

3.6 Catalytic activity results

3.6.1 Effect of borate species on catalytic activity

In order to evaluate the effect of borates on the catalytic activity of (Ni,Co) NPs the catalytic behavior of the following samples A, B, D and E, all with a Ni/Co ratio ≈ 1 but separated with different procedures, will be compared, after tests at a GHSV of 324000 h^{-1}. It has to be remarked that the following order, in terms of borates concentration on the fresh samples, has been evaluated by means of IR spectroscopy (Figure 2): D > E > A > B).
In Table 2, the catalytic activity of the sample D is summarized. This sample, according to XRD on the annealed sample, contains both crystalline borate and the metals solid solution. By looking at the catalytic activity, it has a limited ethanol conversion at low temperature (i.e.

1% at 523 K) with acetaldehyde as the only detectable product, produced by ethanol dehydrogenation.

(4) $CH_3CH_2OH \rightarrow CH_3CH{=}O + H_2$

A temperature increase (573 K) produces an increased ethanol conversion with the presence of acetaldehyde, methane and CO, being produced by ethanol catalytic decomposition.

(5) $CH_3CH_2OH \rightarrow CH_4 + CO + H_2$

likely with the intermediate formation and further decomposition of the same acetaldehyde

(6) $CH_3CH{=}O \rightarrow CH_4 + CO$

At 673 K, ethanol is completely converted and a hydrogen yield of 44% is achieved, with methane, CO and CO_2 selectivities of ~30% each, suggesting that both ethanol decomposition (5) and ethanol steam reforming (ESR, 7) are occurring.

(7) $CH_3CH_2OH + 3\ H_2O \rightarrow 2\ CO_2 + 6\ H_2$

Small amounts of acetaldehyde and acetone are also observed suggesting that ethanol dehydrogenation reaction (4) still occurs while aldol condensation of acetaldehyde followed by dehydrogenation and decarbonylation also occurs to some extent. A further temperature increase to 773 K produces an increased CO_2 selectivity by a faster ESR reaction and a maximum hydrogen yield of 69%. A slight deactivation is observed when comparing the ascending and descending temperature experiments, suggesting that carbon deposition may occur resulting in deactivation of ethanol decomposition more than ESR. However, at 573 and 523 K the situation is similar to the one reported for the increasing temperature experiments with acetaldehyde as the main product.

The sample E after annealing is mainly composed by the cubic (Ni,Co) alloy, as discussed in paragraph 3.2, while the as cast sample presents the characteristic features of surface borates when characterized through FT-IR. In this case, the catalytic activity, summarized in Table 3, is similar to the one reported for D at 523 and 573 K while at 673 K ethanol conversion is still far from 100% (i.e. 93%) and hydrogen yield approaches 40%. At the maximum reaction temperature, a hydrogen yield of 65% is obtained and some deactivation is again present in the decreasing temperature experiment.

The catalytic activity of sample B is summarized in Table 4. Despite the same applied conditions, in this case, a remarkable ethanol conversion is already obtained at 523 K with acetaldehyde as main product (89% selectivity) together with CO and methane (6% and 4% selectivities, respectively) as by-products. As observed in all other cases, ethanol

conversion increases by increasing the reaction temperature but, in this case, a slightly higher hydrogen yield (75%) is obtained mainly at the expenses of methane and CO selectivities. By lowering the reaction temperature at 673 K, the catalyst loses 10% of its catalytic activity and again this is assignable to the reduced ethanol decomposition activity, since the constant value observed for CO_2 selectivity. Below 673 K, ESR activity is nil (at 573 K, 6% CO_2 selectivity) and the main reaction is again the dehydrogenation of ethanol to acetaldehyde and its further decomposition.

The sample showing the lowest amount of borates (A, Table 5) is even more active at low temperature in the production of acetaldehyde, CO and CH_4 (32% ethanol conversion) but its activity it is slightly reduced at 573K (10% ethanol conversion) with an analogous products distribution. At 673 K, the conversion has the worst values (71%) among the compared catalysts due mainly to the lowered activity in acetaldehyde decomposition reaction. An opposite situation is observed at the maximum tested temperature where the best hydrogen yield is observed (82%). In the decreasing temperature experiments, the observed catalytic behavior is similar to the one reported for the other samples with a non-negligible deactivation for the investigated system as already reported of Co [17].

The comparison of the data concerning samples D, E, B and A, shows, according to IR analysis, a decrease of the amount of borate species (D > E > B > A), and a roughly inversed steam reforming activity at 773 K (H_2 yields 68% ≈ 65% < 75% < 81%, for D, E, B and A, respectively). Thus, a negative role for the presence of borate species is confirmed. The same trend is also found for ethanol conversion at 523 K (0.8 % (D) < 4.0 % (E) < 18.0 % % (B) < 32.4 % (A)) where acetaldehyde is by far the main product in all cases. This suggests that the sites allowing acetaldehyde dehydrogenation at low temperature can become sites for steam reforming at a temperature sufficiently high to activate water.

It seems interesting to compare the behavior of sample D, the richest in borates, with that of a very similar pure Cobalt sample (Ni free), reported in reference [17] (i.e. denoted as D). The comparison shows that a strong enhancement of catalytic activity at 673 K is achieved by substituting half of the Co amount with Ni. At this temperature, an ethanol conversion of 100% (Y_{H_2} =44%) is achieved with the bimetallic catalyst against the 60% for the monometallic Co NPs (Y_{H_2}=17%), with the main production of C1 gases (CO, CH_4 and CO_2, selectivities 30% approx.) and the detection of extremely low amounts of acetaldehyde, which is instead the main product for bare CoNPs. A second effect can rely on the reduced deactivation observed upon the decreasing temperature experiment; in fact, by comparing

the data at 673 K, bimetallic NPs reduce their activity by a 20% that rise up to 50% for monometallic Co NPs.

Again by comparing the behavior of these two borate-rich samples, hydrogen yield at the highest tested temperature is similar in the two cases and this is mainly due to the still uncomplete conversion of ethanol over monometallic borate-rich Co NPs that compensate the higher CH_4 selectivity observed for bimetallic borate-rich (Co,Ni) NPs. This might suggest that the addition of Nickel to the formulation of Co nanoparticles can partially overcome to the deactivation induced by the presence of borates, which can, on the other hand, protect the NPs from ageing in oxidant environment, i.e. open air, as discussed in the following paragraph.

3.6.2 Effect of B/Co ratio and of the presence of borides (samples C and B as synthetized and after ageing)

The effect of B/Co has been investigated by considering samples with the same Ni/Co ratio ≈1 and a comparable amount of borates as determined on fresh catalysts by means of IR spectroscopy. As previously reported, sample B is characterized by a B/Co atomic ratio ~ 1 and, after annealing, contains the cubic metal alloy and the boride BMe_3. After annealing, sample C shows only the characteristic cubic metal alloy solid solution, while the B/Co has been estimated to be ~ 0.43 on the fresh nanopowder.

Tables 4 and 6 report the catalytic activity data of samples B and C, respectively. The catalytic activity of these two samples is similar, suggesting that the presence of metal boride phase has a negligible effect.

These two catalysts have also been tested after ageing, performed by leaving (Ni,Co) NPs in open air for 30 days. Ageing of sample C did not significantly change the IR spectrum, where the band assignable to borates at 1410 cm^{-1} did not change its absorbance. As reported in Table 7, compared to Table 6, the catalytic activity of sample C did not change significantly after ageing. In order to strengthen ageing process, the same catalyst has been exposed to ambient air at 473 K for 10 minutes; also in this case no modification of the IR spectrum and of the catalytic activity (not reported) have been observed.

A complete different situation is observed in the IR spectrum of the catalyst B, where a drastic increase of the band at 1410 cm^{-1} is evident after ageing (Fig. 7), and also results in a strong decrease of catalytic activity (not reported here).

The behavior of sample C suggests that, despite the lower catalytic activity of borate containing (Ni,Co) NPs, a protective effect can be played by surface borate in avoiding ageing of nanoparticles (e.g. irreversible poisoning).

Thus, as already reported for CoNPs, the presence of boron in the form of borates in the fresh nanoparticles has an evident negative effect (reduction of ethanol conversion and hydrogen yield) in the catalytic activity while a positive one is evidenced in the reduced ageing of this materials when aged or manipulated in a non-controlled atmosphere. On the other hand, the presence of boride species does not influence negatively the catalytic activity, but the catalyst is more prone to deterioration by ageing.

3.6.3 Effect of Ni/Co ratio (samples A, F and G).

To evaluate the effect of Ni/Co ratio, catalysts with the same B/Co ratio and quite comparable borates content have been considered. The compared samples are: A (Ni/Co=1), F (Ni/Co=0.52) and G (Ni/Co=0.26). Additionally, Ni-free Co sample from our previous work (sample A labeled in [17]) is also taken into account, while data on a Co-free Ni sample are considered, also reported previously [15].

In Table 8, the data for sample G are reported. The comparison with the data concerning sample A (Table 5) shows that sample G is definitely more active at any temperature, with higher performances in ESR at 773 K, providing 87 % yield in H_2 at 773 K. This sample also shows full selectivity to acetaldehyde at 523 K, but high selectivities to methane (23-30 %) at 673 K. The data concerning sample F (not shown) are intermediate between those of samples A and G. If compared with Co-free Ni NPs [15], catalyst G appears to be definitely more selective to ESR, with lower methane production. In contrast, if compared with Ni-free Co NPs [17~~15~~] sample G is more active with a lower acetaldehyde production.

It seems that the (Co,Ni) bimetallic nanoparticles may improve the catalytic behavior, with a reduction of the ethanol (or acetaldehyde) decomposition activity of nickel, and an improving of the activity of cobalt.

In order to further check the role of Nickel in the bimetallic formulation, the GHSV has been reduced by a factor five (from 324000 h^{-1} to 51700 h^{-1}), and experiments have been reported for 523 K. As previously reported for Co NPs [17], a decrease of space velocity is not affecting high temperature performances, while a strong effect is detectable at low temperature suggesting that, also in this case, the experiments are conduced in a proper kinetic regime. In these conditions, ethanol conversion that is 0% for Co NPs, rises at 42% for (Co,Ni) NPs (Ni/Co =0.26) and is 92% for Ni NPs [15]. However, a complete change in

product distribution is also observed in these conditions (see Figure 8): for (Co,Ni) NPs the main products, with an almost complete selectivity, is acetaldehyde with a small coproduction of CO and CH_4, while for Ni NPs the main products are methane and CO while yield to acetaldehyde is found to be lower than 12%. This further confirms that Ni addition may increase catalytic activity of monometallic Co NPs. Monometallic CoNPs do not catalyse ethanol decomposition at low temperature; this reaction is faster on Ni catalysts.

3.7 Characterization of the catalytic materials after catalysis.

After catalysis, the exhaust catalysts have been characterized by means of XRD and FE-SEM.

In Figure 9, the diffractograms of representative catalysts after increasing and decreasing temperature experiments are reported. It is possible to distinguish for all of them two different crystalline phases; the former one is the (Co,Ni) solid solution with a cubic structure (cF4-Cu) while the latter is assignable to the presence of graphitic carbon (2theta=25° and 44°). According to our previous studies on unsupported Co [17] and Ni [15] nanoparticles, the XRD of the exhaust catalysts present the Cubic structure for Co while a metastable hexagonal (hcp) structure, stabilized by the presence of Carbon, for Ni. However, according to the present study, bimetallic (Co,Ni) NPs are found with the cubic structure with no evidence of Ni hcp structure, supporting the formation of a solid solution, between the two metals. Representative FE-SEM micrographs are shown in Figure 10, where it is possible to identify well dispersed nanoparticles in a matrix of carbon nanotubes. Also SEM-EDX analysis on bright particles (as observed in figure 10 (right) with BSE signal) reveals after catalytic tests the co-presence of both Ni and Co, suggesting that no preferential rearrangement (i.e. preferential growth of carbon on Ni, with sequential segregation) occurs in this case.

4 Conclusions.

The data described and discussed above allow to obtain the following conclusions:

1. The reduction of Ni and Co chlorides by sodium borohydride allows to produce (Co,Ni) bimetallic nanoparticles with a quite homogeneous particle size of about 20 nm. These particles, originally amorphous, crystallize into the cubic structure (cF4-Cu) solid solution alloy after annealing in inert atmosphere.

2. The washing and separation procedures leave boron impurities in the sample. The separation procedure and thermal treatments determines the amount and state of boron impurities, mainly in the form of borates or borides.
3. The bimetallic nanoparticles are active in ethanol conversion in the presence of steam. The presence of boron impurities, however, affects the catalytic activity. The presence of borate species is associated to weaker catalytic activity. However, the catalysts can be aged without losing activity. Reversely, the presence of borides does not affect activity but is associated to catalysts that lose activity upon ageing.
4. For low Boron catalysts, the addition of Nickel to Cobalt nanoparticles improves the catalytic activity in ethanol steam reforming allowing yields as high as 87 % at 773 K, at high space velocities (GHSV 324000 h^{-1}).
5. In particular, the addition of Ni to Co increases catalytic activity while the presence of Co reduces the tendency of Nickel to produce methane by ethanol decomposition. Consequently, the sample with Ni/Co = 0.26 appears to be a better catalyst than pure Ni and pure Co, with very high activity at very low contact times. The performances of these catalytic unsupported nanoparticles appear to be better than those of conventional supported catalysts.
6. Carbonaceous materials, such as carbon nanotubes and graphitic carbon, form on the catalyst surface upon reaction.
7. Metallic particles are active in ESR even without any support. This implies that the surfaces of both nickel and cobalt particles, and their alloys, possess in reaction conditions the functionalities for activating both water and ethanol. The effect of the supports is most likely an indirect one, modifying the p'hysical properties of the metal particles.

Figure captions:

Figure 1: XRD of annealed sample under investigation. In the inset, the peak at 2theta=76.3° has been magnified, showing the formation of the alloy between Ni and Co.

Figure 2: IR spectra of fresh investigated catalysts in the characteristic skeletal region (1600-400 cm^{-1})

Figure 3: FE-SEM micrographs in secondary electrons for representative samples: C (3a), B (3b) and G (3c).

Figure 4: HAADF-STEM images and corresponding STEM-EDX maps of Co and Ni for samples (a) C and (b) B.

Figure 5: (a) HAADF-STEM image of sample A and (b,c) elastically filtered (zero-loss) TEM images of samples (b) F and (c) G.

Figure 6: Room temperature magnetic hysteresis cycles of E and A samples.

Figure 7: IR of fresh and aged B and C samples

Figure 8: Effect of gas space velocity and Ni content in (Co,Ni) NPs in ESR condition at 573 K

Figure 9: XRD of exaust samples

Figure 10: FE-SEM micrographs of a representative exaust sample (G): image acquired collecting secondary electrons on the left and back-scattered electrons on the right.

Table 1. Summary of catalysts properties

Sample notations	Separation method	Ni/Co nominal composition	Ni/Co measured composition	B/Me (Me=Co,Ni) measured ratio	A $(BO_3)^{3-}$
A	filtration	1	1	1	0.13
B	filtration	1	1	1	0.23
C	sonication	1	1	0.43	0.24
D	centrifugation	1	n.m.*	n.m.*	0.4
E	sonication	1	n.m.*	n.m.*	0.25
F	filtration	0.50	0.52	1	0.13
G	filtration	0.25	0.26	1	0.18
* n.m. stays for not measured					

Table 2: Catalytic activity of sample D in ESR at GHSV 324000 h^{-1}, ethanol and water conversion, hydrogen yield and selectivities to carbon products.

T (K)	X C_2H_6O	X H_2O	Y H_2	S CH_4	S CO	S CO_2	S CH_2CH_2	S CH_3COH	S CH_3COCH_3	S $(CH_3CH_2)_2O$
523	1%	0%	0%	0%	0%	0%	0%	100%	0%	0%
573	15%	0%	3%	2%	3%	0%	0%	95%	0%	0%
673	100%	16%	44%	29%	32%	31%	2%	5%	1%	0%
773	100%	32%	69%	21%	12%	68%	0%	0%	0%	0%
673	83%	15%	39%	21%	20%	39%	3%	16%	0%	0%
573	15%	1%	3%	4%	6%	6%	0%	80%	0%	4%
523	3%	0%	1%	0%	0%	0%	0%	100%	0%	0%

Table 3: Catalytic activity of sample E in ESR at GHSV = 324000 h^{-1}, ethanol and water conversion,
hydrogen yield and selectivities to carbon products.

T (K)	X C_2H_6O	X H_2O	Y H_2	S CH_4	S CO	S CO_2	S CH_2CH_2	S CH_3COH	S C_3H_6O
523	4%	0%	1%	0%	0%	0%	0%	100%	0%
573	13%	0%	2%	3%	4%	0%	0%	93%	0%
673	93%	13%	39%	28%	34%	27%	0%	10%	2%
773	100%	31%	65%	24%	10%	66%	0%	0%	0%
673	81%	12%	33%	26%	26%	30%	2%	16%	1%
573	15%	0%	3%	6%	8%	2%	0%	84%	0%
523	4%	0%	1%	2%	3%	2%	0%	93%	0%

Table 4: Catalytic activity of sample B in ESR at GHSV 324000 h^{-1}, ethanol and water conversion, hydrogen yield and selectivities to carbon products.

T(K)	X C_2H_6O	X H_2O	Y H_2	S CH_4	S CO	S CO_2	S CH_3CHO	S C_3H_6O
523	18%	0%	3%	4%	6%	1%	89%	1%
573	28%	1%	6%	3%	6%	3%	88%	0%
673	97%	17%	48%	24%	36%	32%	7%	1%
773	100%	36%	75%	17%	8%	75%	0%	0%
673	83%	14%	39%	18%	27%	31%	22%	1%
573	8%	0%	2%	4%	6%	3%	87%	0%
523	4%	0%	1%	0%	0%	0%	100%	0%

Table 5: Catalytic activity of sample A in ESR at GHSV 324000 h^{-1}, ethanol and water conversion, hydrogen yield and selectivities to carbon products.

T(K)	X C_2H_6O	X H_2O	Y H_2	S CH_4	S CO	S CO_2	S CH_2CH_2	S CH_3CH_3	S CH_3CHO	S C_3H_6O
523	32%	0%	6%	5%	8%	1%	0%	0%	85%	1%
573	10%	0%	2%	3%	6%	2%	0%	0%	89%	0%
673	71%	10%	30%	14%	27%	23%	1%	0%	34%	1%
773	100%	39%	81%	12%	7%	81%	0%	0%	0%	0%
673	55%	22%	22%	20%	40%	17%	1%	2%	20%	1%
573	13%	0%	3%	4%	8%	4%	0%	0%	84%	0%
523	2%	0%	0%	1%	2%	0%	0%	0%	96%	0%

Table 6: Catalytic activity of sample C in ESR at GHSV 324000 h^{-1}, ethanol and water conversion, hydrogen yield and selectivities to carbon products.

T (K)	X C_2H_6O	X H_2O	Y H_2	S CH_4	S CO	S CO_2	S CH_2CH_2	S CH_3CHO	S C_3H_6O	S $C_4H_8O_2$	S CH_3COOH
523	38%	0%	7%	4%	6%	0%	0%	89%	1%	0%	0%
573	13%	0%	3%	3%	5%	3%	0%	88%	0%	1%	0%
673	94%	13%	42%	23%	43%	22%	1%	8%	1%	0%	1%
773	100%	29%	62%	25%	13%	62%	0%	0%	0%	0%	1%
673	83%	13%	38%	18%	32%	27%	1%	19%	2%	0%	1%
573	14%	0%	3%	4%	8%	4%	0%	82%	0%	2%	0%
523	4%	0%	1%	1%	2%	2%	0%	94%	0%	0%	0%

Table 7: Catalytic activity of aged sample C in ESR at GHSV 324000 h^{-1}, ethanol and water conversion,
hydrogen yield and selectivities to carbon products.

T (K)	X C_2H_6O	X H_2O	Y H_2	S CH_4	S CO	S CO_2	S CH_3CHO	S C_3H_6O
523	8%	0%	1%	3%	3%	1%	93%	0%
573	14%	0%	3%	3%	4%	1%	91%	0%
673	94%	12%	38%	26%	36%	23%	12%	1%
773	100%	34%	72%	18%	10%	72%	0%	0%
673	67%	8%	25%	18%	20%	23%	34%	1%
573	12%	0%	2%	3%	4%	4%	88%	0%
523	3%	0%	1%	2%	2%	3%	91%	0%

Table 8: Catalytic activity of sample G in ESR at GHSV 324000 h^{-1}, ethanol and water conversion, hydrogen yield and selectivities to carbon products.

T (K)	X C_2H_6O	X H_2O	Y H_2	S CH_4	S CO	S CO_2	S CH_2CH_2	S CH_3CHO	S C_3H_6O
523	5%	0%	1%	0%	0%	0%	0%	100%	0%
573	13%	0%	2%	3%	5%	0%	0%	92%	0%
673	100%	13%	41%	30%	39%	25%	2%	3%	2%
773	100%	43%	87%	9%	3%	88%	0%	0%	0%
673	88%	10%	34%	23%	32%	21%	1%	9%	0%
573	15%	0%	3%	5%	8%	2%	0%	85%	0%
523	4%	0%	1%	0%	0%	0%	0%	100%	0%

Acknowledgements. The collaboration of Elena Reghitto and Lea Pasquale during the preparation of their master theses is gratefully acknowledged.

This research did not receive any specific grant from funding agencies in the public, commercial, or not-for-profit sectors.

References

[1] Busca G (2014), Heterogeneous Catalytic Materials, Elsevier, pp. 297-344.

[2] Anderson JA, Fernández García M eds. (2011) Supported Metals in Catalysis, 2nd Edition, World Scientific.

[3] Ahmadi M, Mistry H, Roldan Cuenya B (2016) Phys Chem Lett 7:3519-3533.

[4] Bion N, Duprez D, Epron F (2012) ChemSusChem 5:76–84

[5] Nahar G, Dupont V, Biofuels (2012) 3:167-191

[6] Soykal I, Bayrama B, Sohna H, Gawadea P, Miller JT, Ozkan US (2012) Appl Catal A Gen 449:47–58

[7] Domínguez M , Cristiano G, López E, Llorca J (2011) Chem Eng J, 176–177:280-285

[8] Resini C, Herrera Delgado MC, Presto S, Alemany LJ, Riani P, Marazza R, Ramis G, Busca G (2008) Int J Hydr En 33:3728-3735

[9] Busca G, Costantino U, Montanari T, Ramis G, Resini C, Sisani M (2010) Int J Hydr En, 35:5356-5366

[10] Moretti E, Storaro L, Talon A, Chitsazan S, Garbarino G, Busca G, Finocchio E (2015) Fuel 153:166-175

[11] Gharahshiran VS, Yousefpour M (2018) Int J Hydr En 43: 7020-7037.

[12] Rodriguez-Gomez A, Caballero A (2018) Mol Catal 449:122-130

[13] Garbarino G, Wang C, Valsamakis I, Chitsazan S, Riani P, Finocchio E, Flytzani-Stephanopoulos M, Busca G (2015) Appl Catal B Environ174:21-34

[14] Garbarino G, Chitsazan S, Phung TK, Riani P, Busca G (2015) Appl Catal A Gen 505:86-97

[15] Riani P, Garbarino G, Lucchini MA, Canepa F, Busca G (2014) J Mol Catal A Chem 383-384:10-16

[16] Garbarino G, Riani P, Lucchini MA, Canepa F, Kawale S,Busca G (2013) Int J Hydr En 38:82-91

[17] Riani P, Garbarino G, Infantes-Molina A, Rodríguez-Castellón E, Canepa F, Busca G (2016) Appl Catal A Gen 518:67-77

[18] Riani P, Garbarino G, Canepa F, Busca G (2018) J Chem Technol Biotechnol in press

[19] Pearson Crystal Data: Crystal structure database for inorganic compounds, Release 2018, ASM international, the Material Information Society

[20] Verbeeck J, Van Aert S (2004) Ultramicroscopy 101:207-224

[21] Delmastro A, Gozzelino G, Mazza D, Vallino M, Busca G, Lorenzelli V (1992) J Chem Soc Faraday Trans 88:2065-2070

[22] Mazza D, Vallino M, Busca G (1992) J Am Ceram Soc 75:1929-1934

[23] Simagina VI, Komova OV, Netskina OV, in Gromov A, Teipel U, Metal Nanopowders: Production, Characterization, and Energetic Applications (2014) 199-227

[24] Glavee G.N, Klabunde KJ, Sorensen CM, Hadjapanayis GC (1992) Langmuir 8 :771-773

[25] Glavee G.N, Klabunde KJ, Sorensen CM, Hadjapanayis GC (1993) Langmuir 9:162-169.

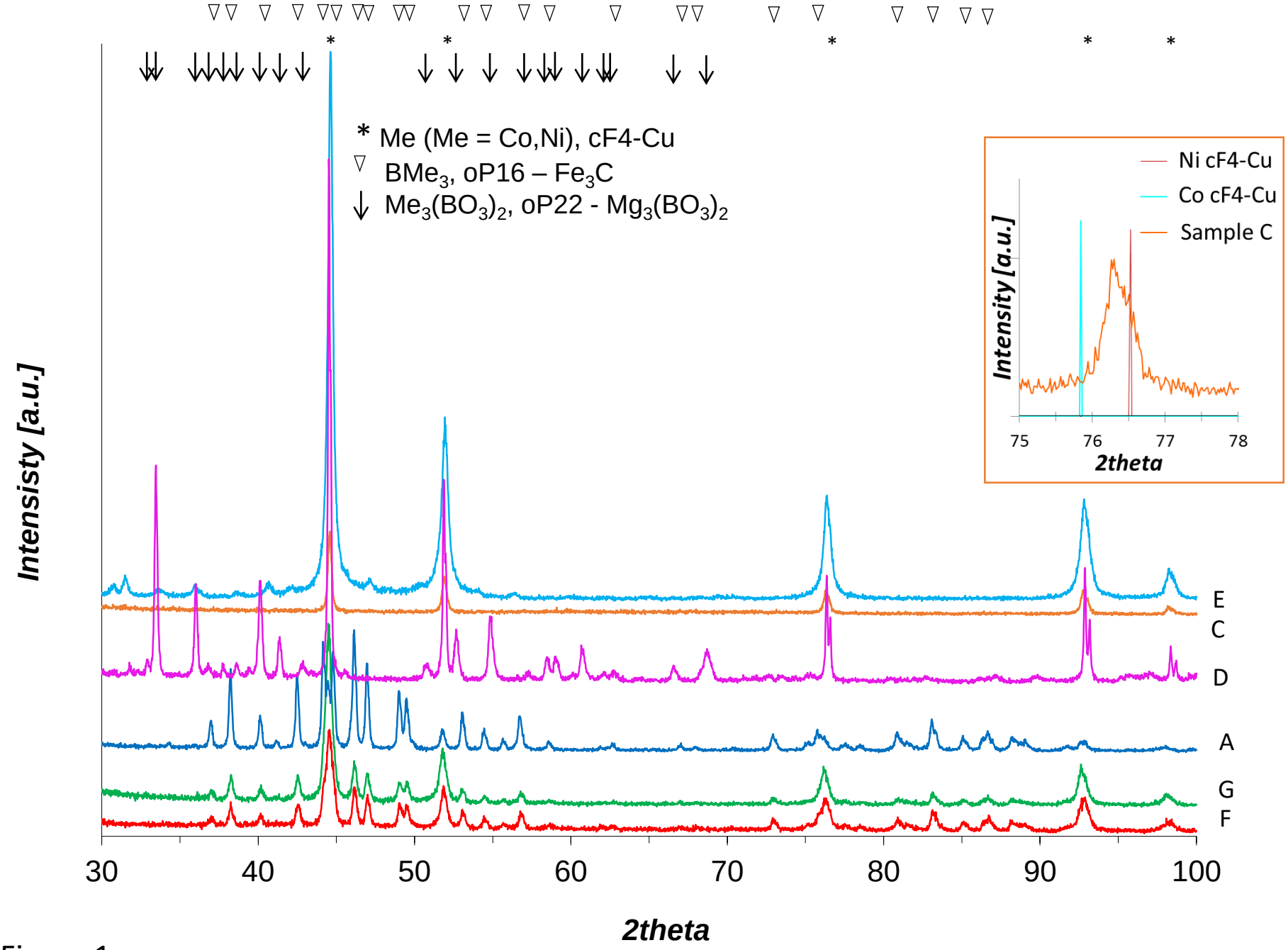
* Me (Me = Co,Ni), cF4-Cu
▽ BMe3, oP16 – Fe3C
↓ Me3(BO3)2, oP22 - Mg3(BO3)2
Intensisty [a.u.]
2theta
30
40
50
60
70
80
90
100
E
C
D
A
G
F
Ni cF4-Cu
Co cF4-Cu
Sample C
Intensity [a.u.]
75
76
77
78
2theta

Figure 1

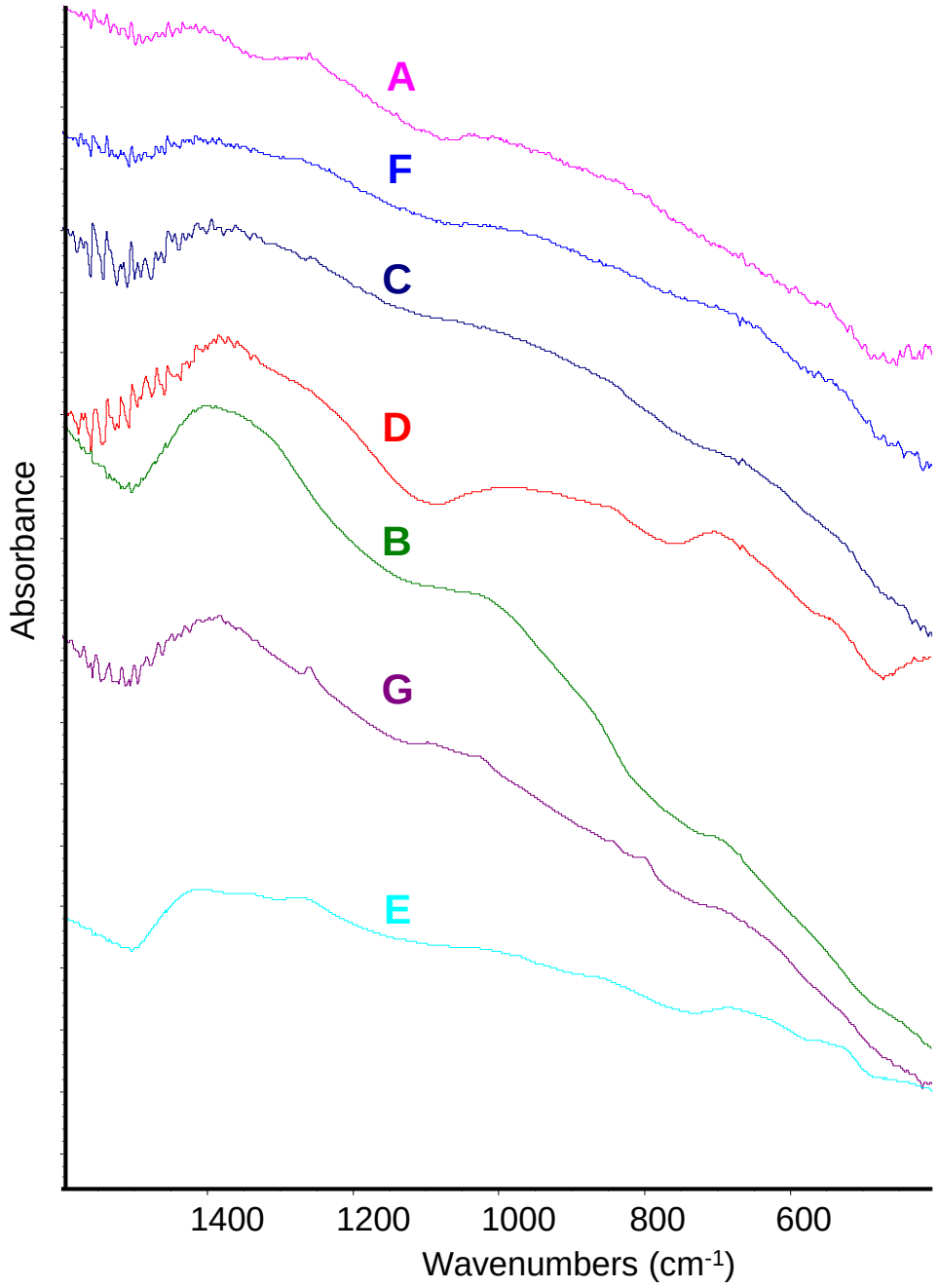

Figure 2

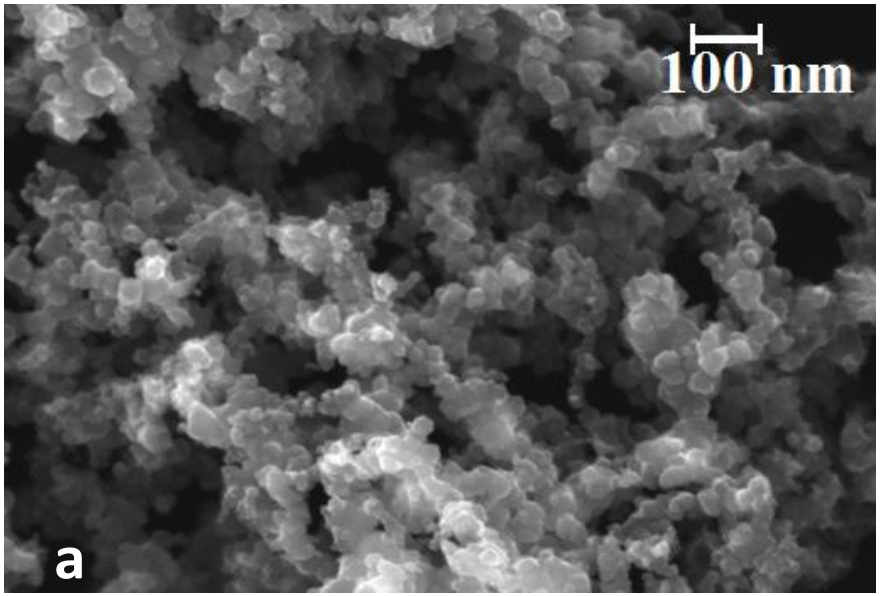

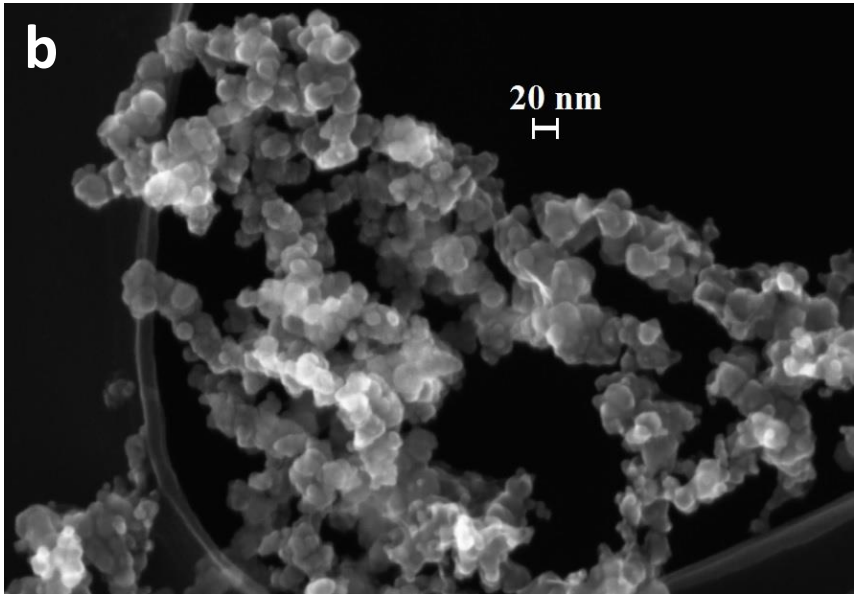

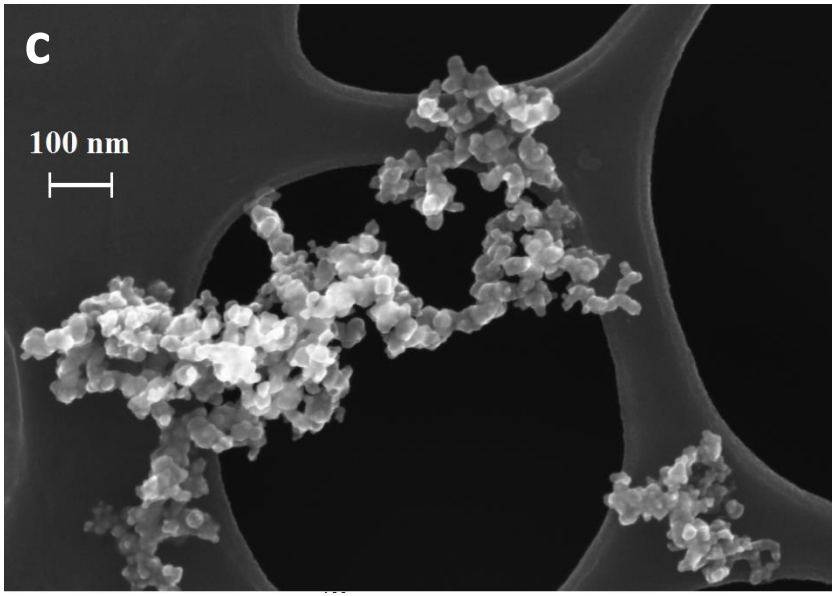

Figure 3

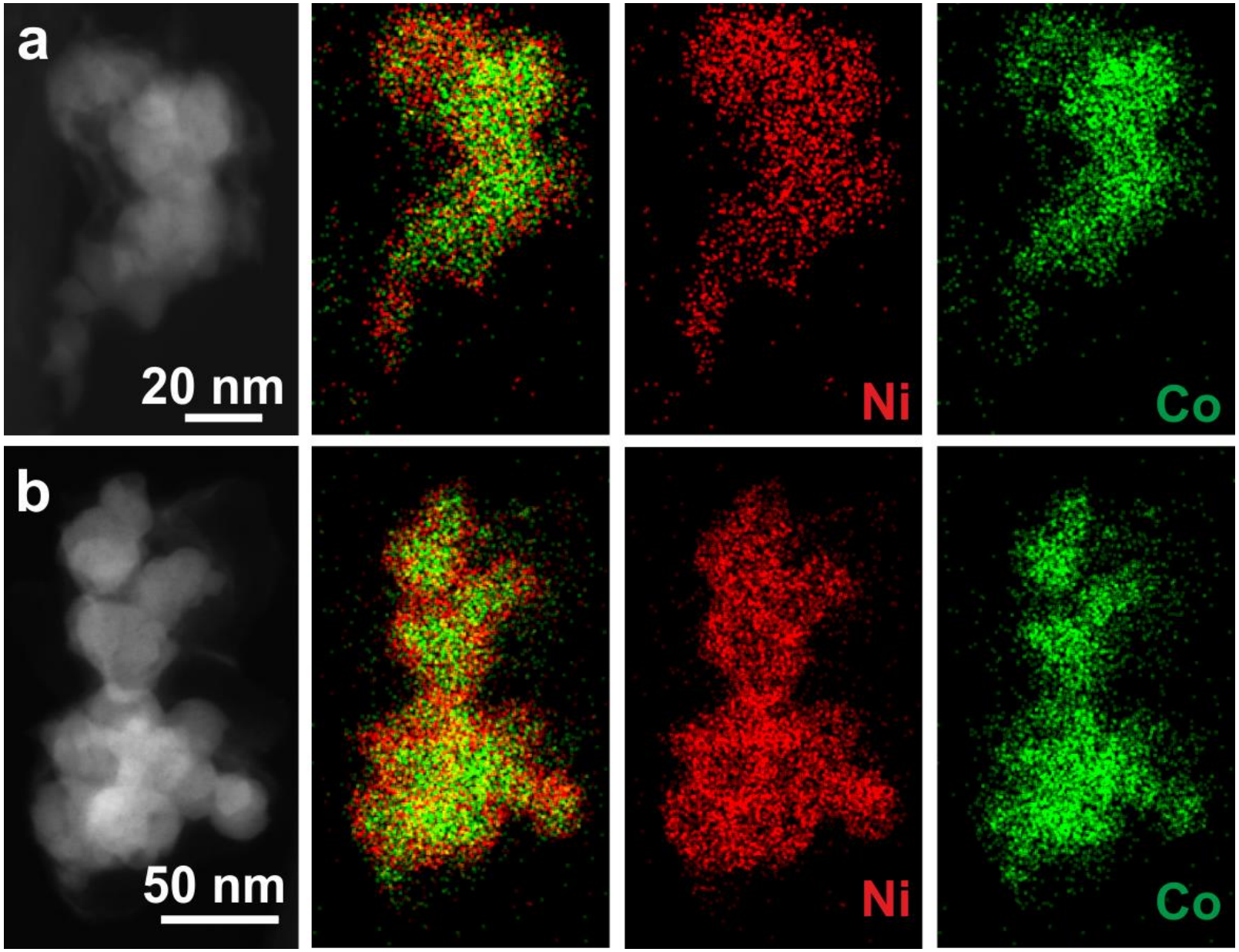

Figure 4

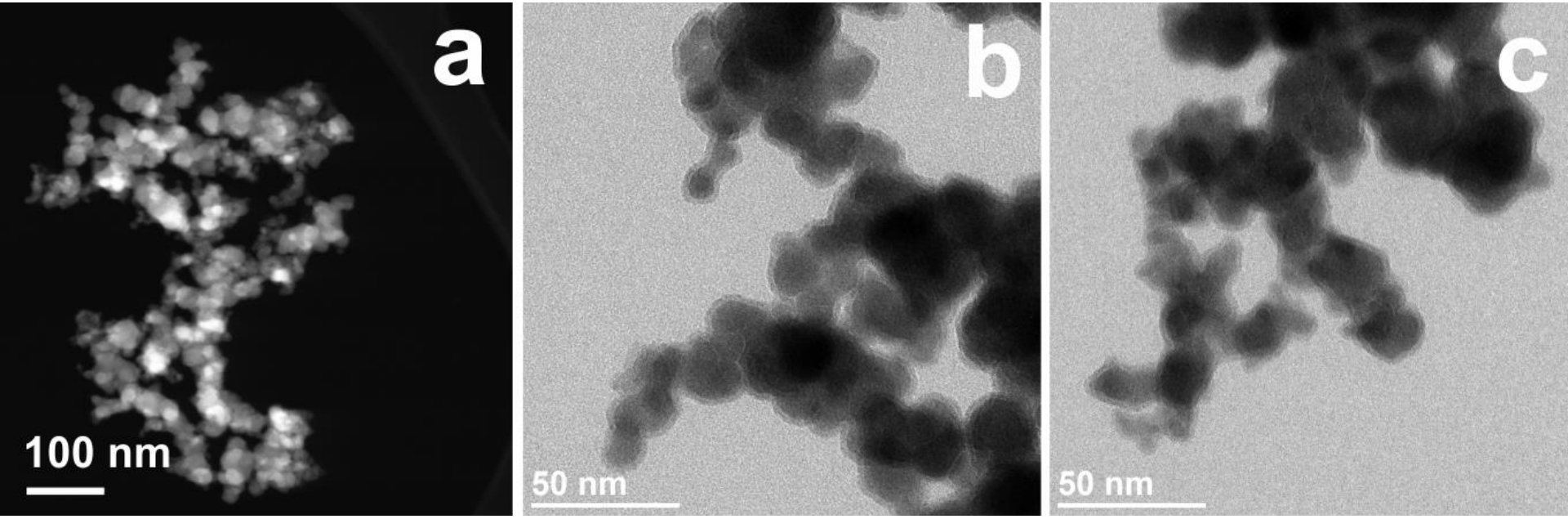

Figure 5

M [ampere*m^2/Kg]

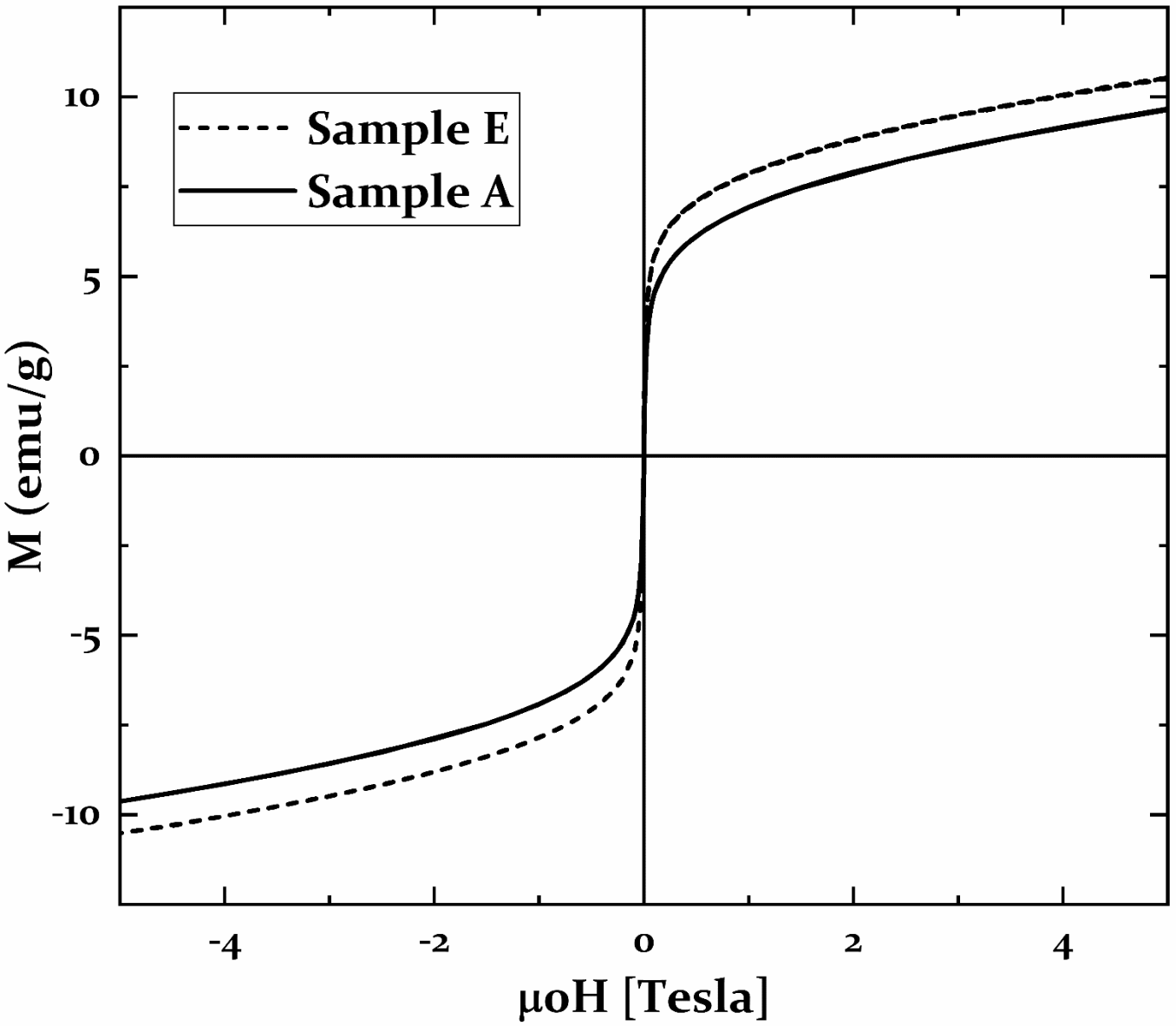

Figure 6

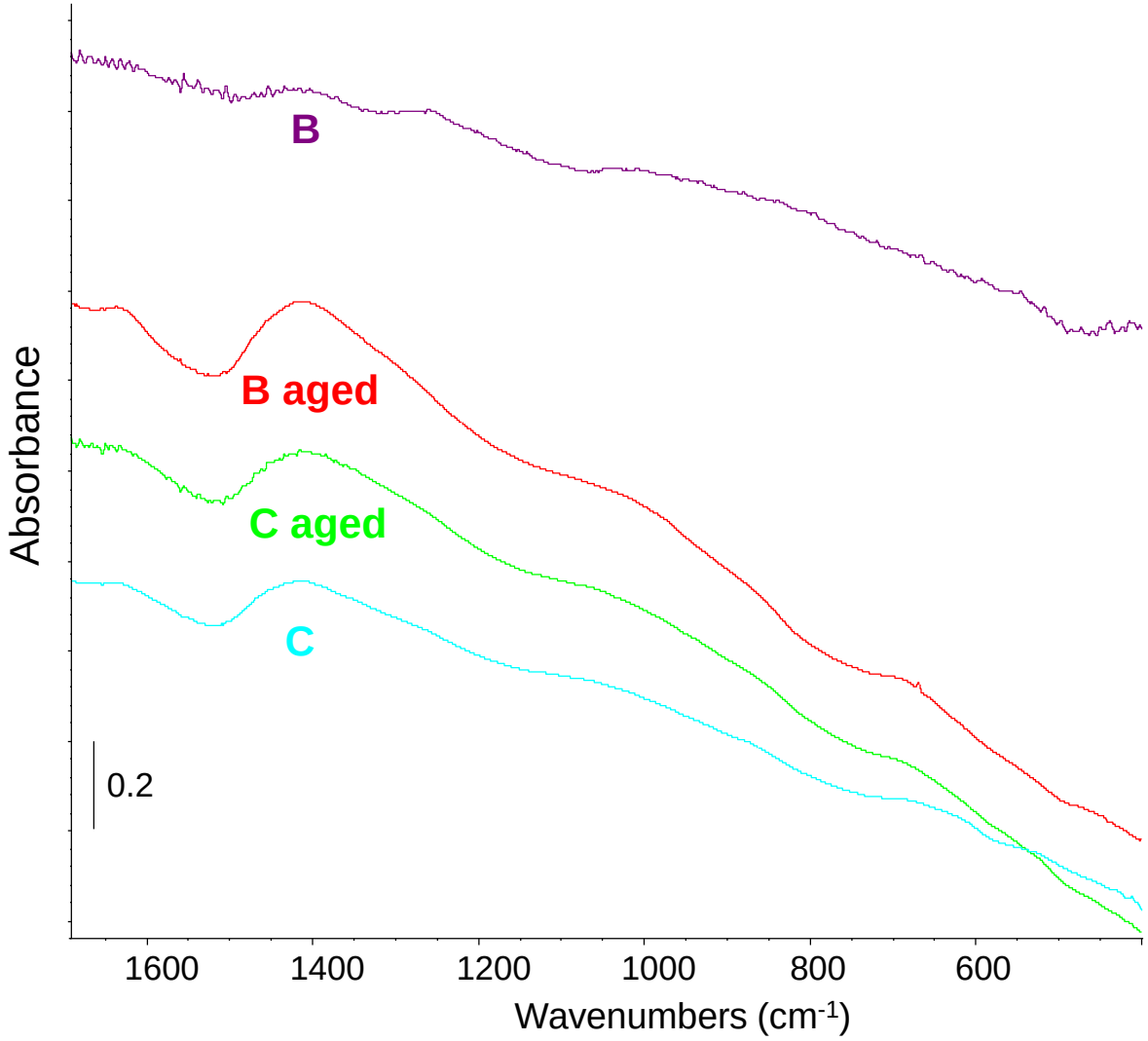
B
B aged
C aged
C
0.2
Absorbance
1600
1400
1200
1000
800
600
Wavenumbers (cm-1)

Figure 7

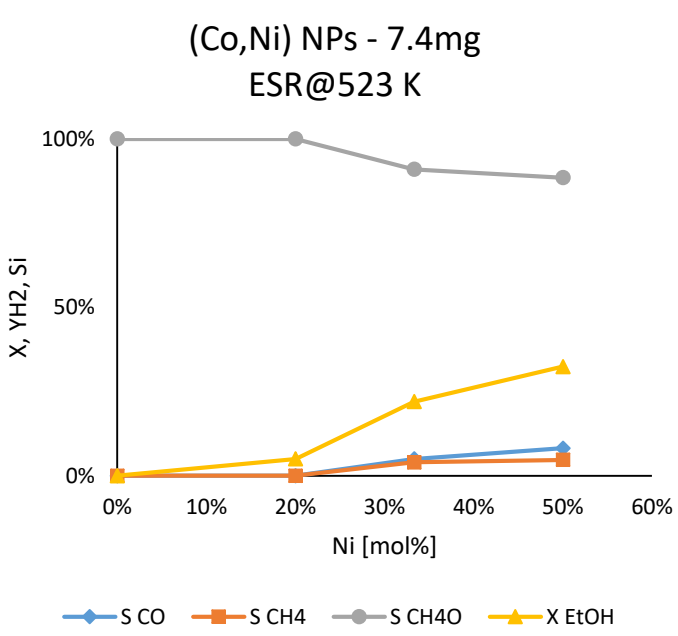
(Co,Ni) NPs - 7.4mg
ESR@523 K
100%
50%
0%
X, YH2, Si
0%
10%
20%
30%
40%
50%
60%
Ni [mol%]
S CO
S CH4
S CH4O
X EtOH

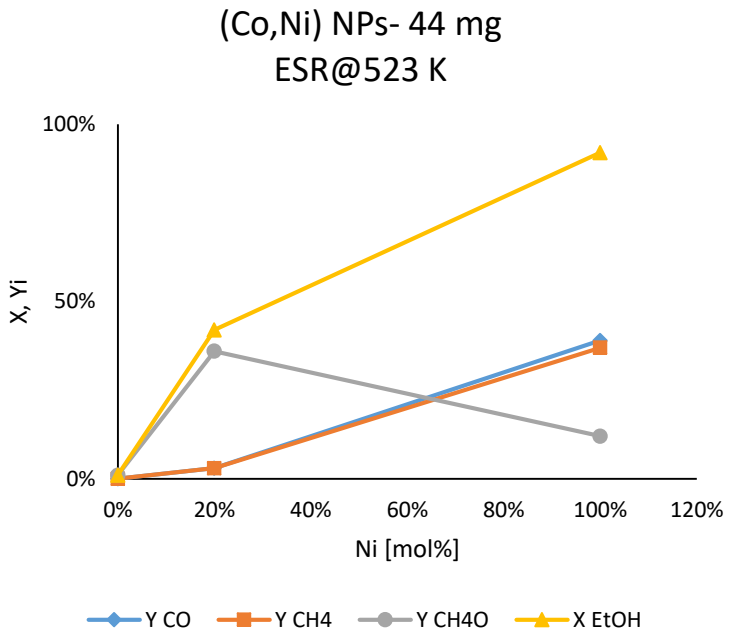
(Co,Ni) NPs- 44 mg
ESR@523 K
100%
50%
0%
X, Yi
0%
20%
40%
60%
80%
100%
120%
Ni [mol%]
Y CO
Y CH4
Y CH4O
X EtOH

Figure 8

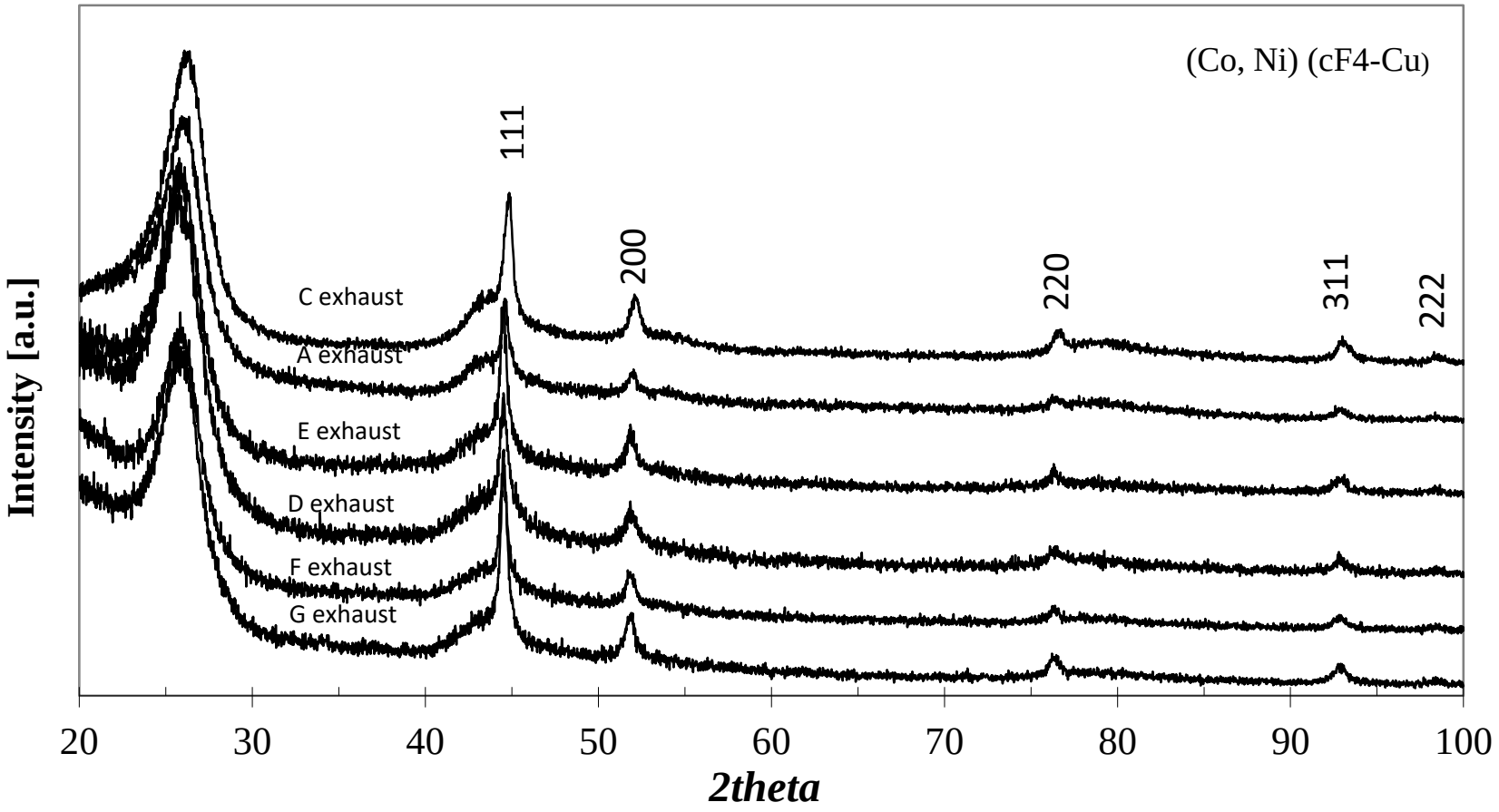
(Co, Ni) (cF4-Cu)
111
200
220
311
222
C exhaust
A exhaust
E exhaust
D exhaust
F exhaust
G exhaust
Intensity [a.u.]
20
30
40
50
60
70
80
90
100
2theta

Figure 9

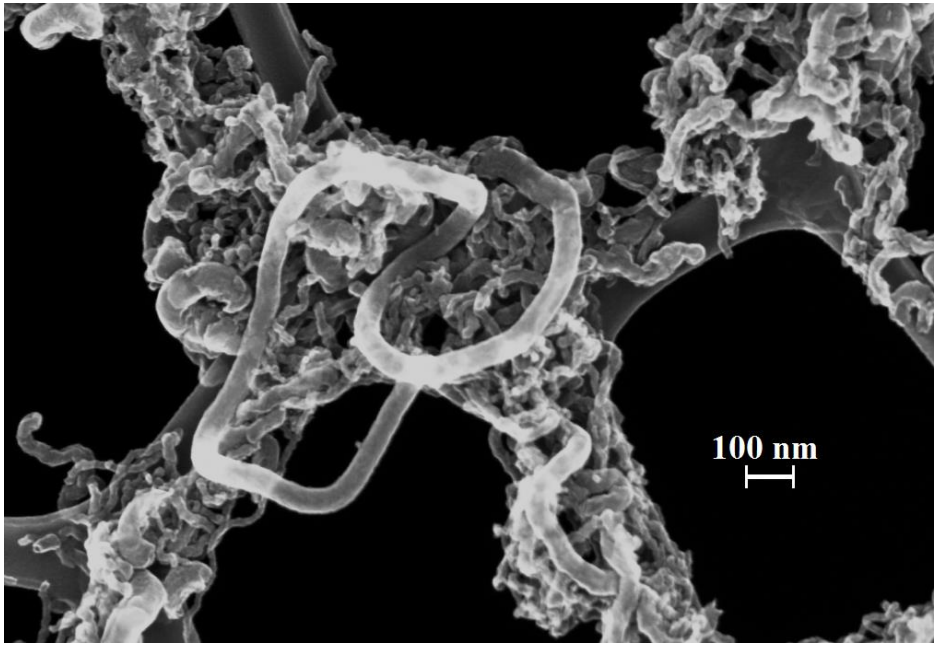

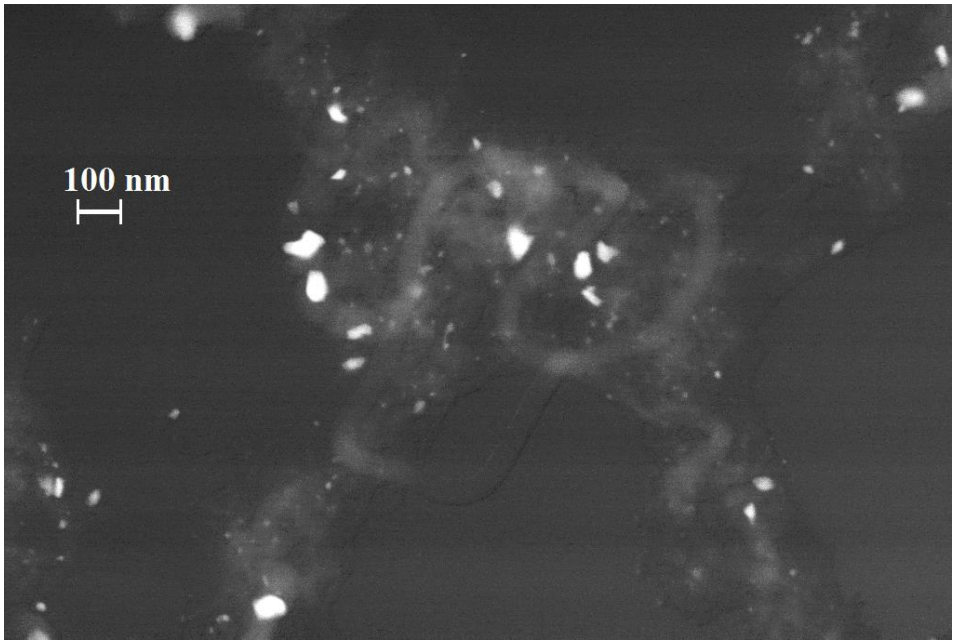

Figure 10